AIP | Physics of Fluids

The spatial evolution of fluctuations in a self-propelled wake compared to a patch of turbulence

Anikesh Pal, Matthew B. de Stadler, and Sutanu Sarkar

Citation: Phys. Fluids **25**, 095106 (2013); doi: 10.1063/1.4819877
View online: http://dx.doi.org/10.1063/1.4819877
View Table of Contents: http://pof.aip.org/resource/1/PHFLE6/v25/i9
Published by the AIP Publishing LLC.

PHYSICS OF FLUIDS **25**, 095106 (2013)

The spatial evolution of fluctuations in a self-propelled wake compared to a patch of turbulence

Anikesh Pal,[a] Matthew B. de Stadler, and Sutanu Sarkar[b]
Department of Mechanical and Aerospace Engineering, University of California San Diego, California 92093, USA

(Received 12 January 2013; accepted 14 August 2013; published online 30 September 2013)

The primary focus of this study is to contrast the influence of the mean velocity profile with that of the initial turbulence on the subsequent evolution of velocity and density fluctuations in a stratified wake. Direct numerical simulation is used to simulate the following cases: (a) a self-propelled momentumless turbulent wake, case SP50 with a canonical mean velocity profile, (b) a patch of turbulence, case TP1 with the same initial energy spectrum as (a), and (c) a patch of turbulence, case TP2 with a different initial energy spectrum with higher small-scale content. The evolution of the fluctuations is found to be strongly dependent on the initial energy spectrum, e.g., in case TP2, the kinetic energy is substantially smaller, and the late-wake vortices are less organized. The effect of the mean velocity field is negligible for mean kinetic energy (*MKE*) of the order 10% of the total kinetic energy and the evolution in this case is similar to a turbulent patch with the same initial energy spectrum. Increasing the *MKE* to 50% shows significant difference from the turbulent patch with the same initial energy spectrum during the initial stages of the evolution, but at later stages the evolution of turbulence statistics is similar. Both the turbulent patch and the momentumless wake show layering and formation of pancake eddies owing to buoyancy. Another objective of the paper is to compare the spatially evolving wake with the temporally evolving approximation when the initial near-wake condition of the temporal approximation is chosen to match the inflow of the spatially evolving model. The mean and turbulent flow statistics are found to agree well between the spatial and temporal computational models under these conditions. © *2013 AIP Publishing LLC*. [http://dx.doi.org/10.1063/1.4819877]

I. INTRODUCTION

The turbulent wake behind a body moving under its own thrust in a stratified fluid is of importance in flows associated with underwater submersibles in naval applications and with swimming marine animals. Experimental studies of a turbulent wake have a long history. Lin and Pao,[1] in their review, concluded that turbulent wakes behave differently depending upon whether the environment is stratified or unstratified. Buoyancy eventually controls the wake by inhibiting vertical motion, leading to wake collapse, propagation of internal gravity waves and, finally, the formation of coherent vortices with primarily horizontal motion. Naudascher,[2] Higuchi and Kubota,[3] and Sirviente and Patel[4] performed experimental investigations of non-swirling, jet-propelled momentumless wakes in an unstratified environment. Higuchi and Kubota[3] found a higher decay rate of the centerline mean velocity defect in a zero-momentum case. After a long gap in published literature, reports of experimental studies of stratified turbulent wakes recommenced in the case of towed bodies using primarily the generic example of a towed sphere.[5–9] Spedding[8] identified three regimes during the evolution of a stratified wake: (a) near-wake (NW) region where the velocity fluctuations are

[a]Electronic mail: anpal@ucsd.edu
[b]Electronic mail: sarkar@ucsd.edu

three-dimensional and buoyancy effects are negligible, (b) non-equilibrium region (NEQ) in which the flow is increasingly influenced by buoyancy resulting in a restratification-driven transfer of potential energy to mean kinetic energy, enhanced internal wave radiation and reduction of the vertical component of turbulence, and (c) quasi two-dimensional (Q2D) region dominated by pancake-like organized vortices with strong interspersed vertical gradients. Spedding[8] also proposed a universal decay law for the mean defect velocity in the three regimes with the decay rate in the NEQ regime being significantly smaller than in either the NW regime or the Q2D regime.

All the numerical turbulence-resolving studies of stratified late wakes are based on a *temporally* evolving model of the wake. Canonical profiles for the mean velocity and turbulence are assumed as initial conditions and the subsequent development of the flow is simulated in a streamwise-periodic domain. Gourley *et al.*[10] performed the first three-dimensional direct numerical simulation (DNS) of initially turbulent wakes with net momentum and found that the formation of coherent structures in the late wake is independent of the initial seeding of the fluctuating fields. Dommermuth *et al.*[11] computed the late wake of a towed sphere in an unstratified and uniformly stratified fluid at $Re = 10^4$ and 10^5 by using large eddy simulation (LES) and found the three stages (NW, NEQ, and Q2D) of the wake evolution and qualitative similarities with laboratory experiments.

Recent simulations of the wake discussed below clearly show that, at high Re, stratified turbulence exhibits substantial enhancement in transport and mixing as suggested by simulations in other configurations.[12,13] Brucker and Sarkar[14] performed DNS at $Re = 10\,000$ and $50\,000$ to compare the evolution of self-propelled and towed wakes in a stratified fluid. Their flow initialization was similar to that used by Dommermuth *et al.*[11] and, although, their results were similar at $Re = 10\,000$, the NEQ regime was found by Brucker and Sarkar[14] to be substantially longer at $Re = 50\,000$ including a phase in which the decay rate of the mean velocity was significantly lower relative to the $Re = 10\,000$ case. The turbulent dissipation rate, ϵ, was also found to exhibit inertial scaling during which $\varepsilon \sim u^3/l \propto t^{-7/3}$. Meunier *et al.*[15] also predict prolongation of the NEQ regime and the late appearance of the Q2D regime for higher Reynolds number via their analytical model based on the self-preservation of the flow. Diamessis *et al.*[16] found a longer NEQ regime at higher Reynolds number and secondary Kelvin-Helmholtz vortices up to $Nt = 100$ when they performed spectral multi-domain-based simulations of the turbulent wake of a towed sphere.

Abdilghanie and Diamessis[17] examined the internal wave field of a stratified turbulent wake, showing that the associated drag increases with increasing Re to about 9% at the highest simulated Re. Interestingly, the radiated waves cluster in a band around approximately 45° propagation angle as in previous laboratory experiments[18,19] and numerical simulations[20,21] of waves emitted by broad-band turbulence. The high- and low-frequency components (correspondingly, high and low propagation angles with respect to the horizontal) of the wave field were found to exhibit preferential viscous decay consistent with the model proposed by Taylor and Sarkar.[20]

A body moving at constant velocity in an unstratified fluid under its own power has a momentumless wake (the integral of the momentum is zero) whose behavior is thought to be qualitatively different from towed wakes. The corresponding situation in the stratified case leads to the integrated momentum in the wake deviating from zero by the momentum carried away by the radiated wave field. In the unstratified case, Tennekes and Lumley,[22] on the basis of a self-similarity analysis that assumes constant eddy viscosity, assert that the centerline defect velocity in a momentumless wake decays faster, $U_0 \propto x^{-4/5}$, relative to the $U_0 \propto x^{-2/3}$ decay of towed wakes. The stratified situation of self-propelled wake evolution into the far wake has been studied only recently.[14,23] Unlike prior findings in the unstratified case, the laboratory data of Meunier and Spedding[23] (available only for $Nt > 50$) showed an irregular mean velocity profile. This finding prompted Meunier and Spedding[23] to conjecture that that the momentumless wake could have a null mean velocity (mean defect velocity is negligible compared to rms velocity fluctuation). These authors also reported that, relative to the towed wake, the momentumless wake had smaller horizontal spacing between vortices, significantly slower decay of horizontal velocity fluctuations, and a higher sensitivity to the initial conditions such as propeller width. Brucker and Sarkar[14] performed the first turbulence-resolving simulation of the momentumless wake, employing the canonical axisymmetric mean profile (see Figure 2(a) of the present paper) having positive and negative velocity lobes that was found in the unstratified situation.[2–4] The momentumless wake was found by Brucker and Sarkar[14] to decay faster than the

corresponding towed wake. The reason was that the momentumless wake, with the same defect velocity and wake radius as a towed wake, has larger mean shear due to the multi-inflectional velocity profile leading to a larger shear production and conversion to turbulence. The authors also found the existence of NW, NEQ, and Q2D regime in the momentumless wake, similar to the towed wake. Voropayev *et al*.[24] studied the wake of a maneuvering body in a stratified fluid experimentally and established that the acceleration of the body transfers significant momentum to the surrounding fluid leading to the formation of coherent dipoles, much larger and different from the ones that form in the late wake at steady state. Pasquetti[25] simulated the far wake of a sphere at $\mathrm{Pr} = 7$, $\mathrm{Re} = 10\,000$, and $\mathrm{Fr} = 25$ by using a temporal approximation, but used initial conditions from a spatially evolving simulation of flow past a sphere. The NW, NEQ, and Q2D regimes in these simulations were found to be compatible with previous experimental results.

de Stadler and Sarkar[26] performed a DNS to predict the effect of excess momentum (up to 40%) on an initially momentumless wake in a stratified fluid. They found that a propelled wake with small to moderate excess momentum causes small to moderate change in the wake development. This result was in contrast to the result of Tennekes and Lumley,[22] derived on the basis of a self-similarity analysis that assumes constant eddy viscosity, that addition of even a small amount of excess momentum to the momentumless wake leads to a disproportionate change towards the longer life time of a towed wake. It is worth noting that the DNS[26] showed that an eddy viscosity cannot parametrize vertical mixing in the stratified wake where the vertical transport of momentum is oscillatory in space and time. Also of interest is the role of mean flow instabilities in the evolution of the coherent structures in the Q2D regime. As discussed earlier, Meunier and Spedding[23] found the momentumless wake to exhibit substantial differences during its development relative to the towed case. They also found that a propelled wake with net momentum as small as 2% of the body velocity momentum differs qualitatively from a momentumless wake.

From the preceding discussion of differences among numerical simulations, laboratory experiments and theory with respect to the evolution of self-propelled wakes, it is clear that the role of a canonical mean profile requires systematic study. These issues motivate us to examine a limiting situation where the mean velocity profile is removed from the initial velocity field while keeping the same initial turbulent fluctuations, and to compare the subsequent evolution of the turbulent patch with that of the original wake. Small-scale turbulence in the near-wake of a body can exhibit differences, for instance, because of differences in boundary layer characteristics. In order to ascertain the impact of the details of the near-wake turbulence, we also perform additional simulations with a different energy spectrum. Since all previous simulations of a stratified wake into the late wake stage have utilized a temporal approximation, we take the opportunity to relax this assumption and instead employ a spatially evolving model with prescribed conditions for near-wake turbulence at the inflow.

Section II provides the formulation, numerical method, and the initial and boundary conditions employed in the problem. Section III describes the methods utilized to analyze the DNS data. Section IV summarizes the evolution of a spatially evolving self-propelled wake and its comparison with a temporal simulation. Section V presents the results from the primary part of this work: comparison between a spatially evolving self-propelled wake and turbulent patches with different spectra. Section VI is an evaluation of the effect of increasing the amount of fluctuation energy residing in the small scales on the subsequent evolution of the self-propelled wake. Conclusions drawn from the present study are given in Sec. VII.

II. FORMULATION

There are two ways of modeling the self-propelled turbulent wake computationally: in a frame where the flow statistics evolve temporally or in a frame where they evolve spatially. The temporally evolving model, universally adopted in past simulations of the stratified turbulent far-wake, approximates the spatially evolving model by neglecting the streamwise evolution of the mean velocity and is often made because the periodic boundary conditions that can then be used significantly lower the simulation time (equivalently computational cost) of calculating Reynolds averages. In the present paper, we will employ the spatially evolving model for understanding the role of mean velocity

profile and turbulent spectra. We will also show a comparison of results from one spatially evolving model of a self-propelled wake with those from a corresponding temporally evolving model. In the wake simulated here, the downstream distance x relative to the body in the spatially evolving model is related to time t in the temporally evolving model by $x = U_\infty t$ where U_∞ is the background velocity of the fluid. As in previous studies of the far-wake, the body and the details of boundary layer separation are not simulated.

A. Governing equations

The three dimensional conservation equations for mass, momentum, and density subject to the Boussinesq approximation for an unsteady incompressible flow are

continuity:

$$\frac{\partial u_k^*}{\partial x_k^*} = 0, \tag{1}$$

momentum:

$$\frac{\partial u_i^*}{\partial t^*} + \frac{\partial (u_k^* u_i^*)}{\partial x_k^*} = -\frac{1}{\rho_0}\frac{\partial p^*}{\partial x_i^*} + \nu \frac{\partial^2 u_i^*}{\partial x_k^* \partial x_k^*} - \frac{\widetilde{\rho^*}}{\rho_0} g \delta_{i3}, \tag{2}$$

density:

$$\frac{\partial \rho^*}{\partial t^*} + \frac{\partial (u_k^* \rho^*)}{\partial x_k^*} = \kappa \frac{\partial^2 \rho^*}{\partial x_k^* \partial x_k^*}. \tag{3}$$

The * superscript denotes dimensional quantities. The density is decomposed into a background density, ρ_0, a linear variation in the x_3 direction, $\bar{\rho}^*(x_3)$, and a fluctuation, $\tilde{\rho}^*(x_i, t)$:

$$\rho^* = \rho_0 + \bar{\rho}^*(x_3) + \tilde{\rho}^*(x_i, t), \tag{4}$$

where $\bar{\rho}^*(x_3) + \tilde{\rho}^*(x_i, t) \ll \rho_0$. Density variation enters the momentum equation only through the buoyancy term. These equations are non-dimensionalized using U_∞ (the body velocity), D (the body diameter), ρ_0. $C^* = \mid \partial \bar{\rho}^*(x_3)/\partial x_3^* \mid_{(t=0)}$ that denotes the constant vertical gradient of background density. The new non-dimensional variables obtained are

$$t = \frac{t^* U_\infty}{D}, \quad x_i = \frac{x_i^*}{D}, \quad u_i = \frac{u_i^*}{U_\infty}, \quad \rho = \frac{\rho^*}{\rho_0}, \quad \tilde{\rho} = \frac{\tilde{\rho}^*}{DC^*}, \quad p = \frac{\tilde{p}^*}{\rho_0 U^2}. \tag{5}$$

Substituting Eq. (5) into (1)–(3), we obtain the non-dimensionalized form as

continuity:

$$\frac{\partial u_k}{\partial x_k} = 0, \tag{6}$$

momentum:

$$\frac{\partial u_i}{\partial t} + \frac{\partial (u_k u_i)}{\partial x_k} = -\frac{\partial p}{\partial x_i} + \frac{1}{Re}\frac{\partial^2 u_i}{\partial x_k \partial x_k} - \frac{1}{Fr^2}\widetilde{\rho}\delta_{i3}, \tag{7}$$

density:

$$\frac{\partial \rho}{\partial t} + \frac{\partial (u_k \rho)}{\partial x_k} = \frac{1}{RePr}\frac{\partial^2 \rho}{\partial x_k \partial x_k}. \tag{8}$$

The relevant non-dimensional parameters are as follows: the Reynolds number, $Re = U_\infty D/\nu$, the Prandtl number, $Pr = \nu/\kappa$, and the body Froude number, $Fr = U_\infty/(N^* D)$ where N^* is the $Brunt - V\ddot{a}is\ddot{a}l\ddot{a}$ frequency or buoyancy frequency defined as $N^* = [-gC^*/\rho_0]^{1/2}$. The non-dimensional buoyancy frequency is $N \equiv Fr^{-1}$. Equations (6)–(8) are solved using DNS to capture the full dynamic range of velocity and density fields.

TABLE I. Parameters for the simulations. SP50 denotes the self-propelled wake with 50% mean kinetic energy and energy spectrum A, TP1 denotes the turbulent patch with spectrum B, and TP2 denotes the turbulent patch with spectrum C. Case SP10 is a self-propelled wake with 10% mean kinetic energy and case TP10 corresponds to a turbulent patch with a similar energy spectrum (spectra E and F, respectively). Cases TP1, TP2, and TP10 do not have an initial mean velocity profile. N_1, N_2, and N_3 represent the number of grid points in the x_1, x_2, and x_3 directions, respectively. L_1, L_2, and L_3 are the length of the domain excluding the sponge region in the respective directions. Spectra A and B are approximately the same. Spectra C and D are similar and have more energy in the small scales as compared to A and B as shown in Figure 1(b).

Case	Re	Fr	Pr	N_1	N_2	N_3	L_1	L_2	L_3	k_0	Spectrum	Simulation type
1. SP50	15 000	3.0	1	4096	384	256	240.38	19.75	12.31	4.0	A	Spatial
2. TP1	15 000	3.0	1	4096	384	256	240.38	19.75	12.31	4.0	B	Spatial
3. TP2	15 000	3.0	1	4096	384	256	240.38	19.75	12.31	8.0	C	Spatial
4. SP50	15 000	3.0	1	2048	384	256	102.5	19.75	12.31	4.0	A	Temporal
5. SP50C	15 000	3.0	1	2048	384	256	102.5	19.75	12.31	7.0	D (∼C)	Temporal
6. SP10	15 000	3.0	1	4096	384	256	240.38	19.75	12.31	4.0	E	Spatial
7. TP10	15 000	3.0	1	4096	384	256	240.38	19.75	12.31	4.0	F	Spatial

B. Numerical scheme and simulation parameters

Results from the different cases listed in Table I will be discussed in detail. The self-propelled wake, case SP50, was simulated using both the temporally evolving model and the spatially evolving model. The turbulent patch (cases TP1 and TP2) was simulated using the spatially evolving model. A fractional step method is used for integrating the Navier-Stokes equation as is briefly described by Brucker and Sarkar[14] and de Stadler and Sarkar.[26] Brucker and Sarkar[14] and de Stadler and Sarkar[26] used Red-black Gauss-Seidel method as a smoother for the multigrid method for solving the Poisson equation for pressure whereas in this study we use the same smoother with successive over relaxation (SOR)[27] to accelerate the convergence of the pressure Poisson equation on stretched grids in all three directions.

1. The temporally evolving model

The computational domain has dimensions of $102.5 \times 19.75 \times 12.31$ (excluding the sponge region in x_2 and x_3) with mesh size of $2048 \times 384 \times 256$. A constant $\Delta x_1 = 0.05$ is used in the streamwise direction. A value of $\Delta x_2 = 0.031$ is used for the central lateral region ($-2 < x_2 < 2$), followed by a block with 10 points that blends into a grid with 1.25% stretching, $\Delta x_{2,\,min} = 0.0326$ and $\Delta x_{2,\,max} = 0.14$. The central vertical region, $-1 < x_3 < 1$, has a uniform grid with $\Delta x_3 = 0.031$, followed by a block with 10 points that blends into a grid with 1.5% stretching, $\Delta x_{3,\,min} = 0.0326$ and $\Delta x_{3,\,max} = 0.12$. Periodic boundary conditions are imposed in the streamwise direction and far field boundary conditions in the spanwise and cross stream direction. After the initial velocity is imposed as described below, the Navier-Stokes equations are advanced in time.

The initial mean velocity profile used for the self-propelled wake cases SP50 and SP10 is identical to the canonical momentumless profile with positive and negative velocity lobes used in the previous work.[14,26] The defect velocity, U_0 for case SP50 is 0.3 whereas for case SP10, $U_0 = 0.11$, implying that SP50 has ∼50% mean kinetic energy of the total in comparison to ∼10% in SP10. As in our previous work, the initial velocity fluctuations are allowed to evolve during an adjustment period while the mean velocity profile is held fixed until the maximum value of $\langle u_1' u_r' \rangle / K \simeq -0.25$, signifying that the cross-correlation has increased to a level typical of turbulent shear flow. The velocity fluctuations at the beginning of the adjustment period are generated as an isotropic divergence-free velocity field in spectral space (Rogallo[28]) which satisfies the spectrum given by

$$E(k) = (k/k_0)^4 e^{-2(k/k_0)^2}. \tag{9}$$

In order to localize the initial turbulence, the fluctuating velocity field u_i' is multiplied with a radial damping function defined as

$$g(r) = a\left[1 + \left(\frac{r}{r_0}\right)^2\right] e^{-\frac{1}{2}\left(\frac{r}{r_0}\right)^2}, \tag{10}$$

where $a = 0.055$ is the maximum initial value of the fluctuation at the centerline, $r = \sqrt{x_2^2 + x_3^2}$ and $r_0 = 0.5$ (half the body diameter).

2. The spatially evolving model

The computational domain has dimensions of $240.38 \times 19.75 \times 12.31$ (excluding the sponge region in x_2 and x_3) with mesh size of $4096 \times 384 \times 256$. We choose the mesh size so that the turbulence energy spectrum is well resolved over the entire domain for all the cases. The streamwise grid is as follows: $\Delta x = 0.045$ until $x_1 = 40$, a 15-point blending region, a stretched grid until $x_1 = 190$ with $\Delta x_{1,\,min} = 0.0451$ and $\Delta x_{2,\,max} = 0.0757$ and, finally, a uniform grid with $\Delta x = 0.0757$. The x_1 grid stretching of 0.02% is mild. The grid spacings in the lateral and vertical directions are identical to those in the temporal model.

For the spatially evolving simulations, inflow-outflow boundary conditions are used in the streamwise direction. An auxiliary simulation generates the flow that is advected into the domain at the inflow boundary. The computational domain for the auxiliary simulation is identical to that employed for the temporally evolving model. The fluctuations for case SP50 are initialized, utilizing divergence-free initial conditions followed by an adjustment to mean shear, as explained in Sec. II B 1. An additional time period of 1.2 D/U_∞ allows for development of buoyancy effects. The turbulent patch cases, TP1, TP2, and TP10, have a constant background flow without shear. The initial velocity fluctuations for the auxiliary simulations in cases TP1 and TP10 are generated by choosing $k_0 = 4$ and by taking $k_0 = 8$ for TP2, in (9), followed by spatial localization using (10). Equations (6)–(8) are solved in their unstratified form for the turbulent patch TP1 for a sufficient amount of time so that its energy spectrum B evolves so as to match the energy spectrum of the self-propelled wake, SP50 (analogous procedure is followed for SP10 and TP10). During this period of adjustment, the spatial profile of the fluctuations is kept fixed. The other turbulent patch simulation, TP2, is also adjusted in a similar manner as TP1 until higher energy is accumulated at smaller scales owing to nonlinear transfer. The initial velocity fluctuations and the initial energy spectrum after the end of the adjustment period for SP50, TP1, and TP2 are shown in Figures 1(a) and 1(b), respectively.

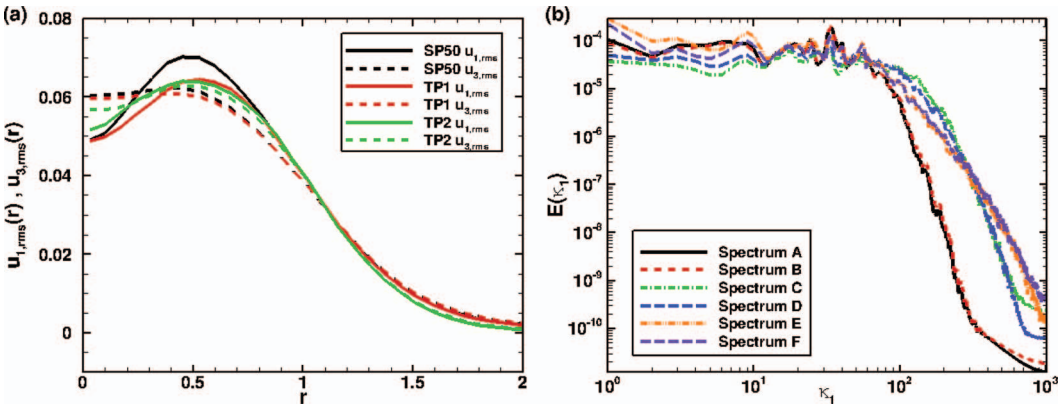

FIG. 1. (a) Radial profiles of streamwise (u_1) and vertical (u_3) *rms* velocity, $u_{2,\,rms}$ matches $u_{3,\,rms}$. (b) *Initial* energy spectra: Spectrum A for SP wake with 50% *MKE*, spectrum B for turbulent patch TP1, spectrum C for TP2, spectrum D for SP wake with 50% *MKE* and the same spectrum as TP2.

Two-dimensional (x_2 and x_3) data planes generated from the auxiliary simulation are advected into the domain to provide inflow conditions. Successive planes from the auxiliary simulation are taken to be the inflow plane of the spatially evolving simulation at successive times with $\Delta t = \Delta x_{auxiliary}/U_\infty$.

The simulation in the spatially evolving domain is initialized as follows: SP50 with a mean wake profile and divergence-free fluctuations, and TP1 and TP2 with divergence-free fluctuations. At the outflow, an extrapolation boundary condition is used for u, v, w, and ρ and a homogeneous Neumann boundary condition is used for pressure. The extrapolation boundary condition uses 2nd order extrapolation to extrapolate the value of the flow variables from the interior of the domain to the outflow boundary, i.e., $\phi^n_{i+1} = 2\phi^n_i - \phi^n_{i-1}$, where "i" is the x-coordinate index and "n" is the time-level.

In order to control spurious reflections from internal gravity waves and other disturbances propagating out of the domain, we use sponge regions near the x_2 and x_3 boundaries, where damping functions gradually relax the value of the variable to its corresponding value at the boundary. These damping functions are added on the right hand side of Eqs. (7) and (8) as explained in Brucker and Sarkar.[14] Note that no sponge layer is used at the outflow as it has been found that the extrapolation boundary condition is sufficient in the present flow to propagate any disturbances out of the domain smoothly. At the spanwise (x_2) and vertical (x_3) boundaries of the sponge region, far field boundary conditions are used:

$$\frac{\partial u_i}{\partial x_2} = 0 \quad (x_2 = \pm L_2/2), \qquad \frac{\partial u_i}{\partial x_3} = 0 \quad (x_3 = \pm L_3/2), \tag{11}$$

$$p = 0 \quad (x_2 = \pm L_2/2), \qquad p = 0 \quad (x_3 = \pm L_3/2), \tag{12}$$

$$\frac{\partial \rho}{\partial x_2} = 0 \quad (x_2 = \pm L_2/2), \qquad \frac{\partial \rho}{\partial x_3} = -\frac{\rho_0 C^*}{D} \quad (x_3 = \pm L_3/2). \tag{13}$$

C. Simulation parameters

Table I shows the simulation parameters for this study. The wake is simulated up to $x_1 \sim 240$, equivalently $Nt \sim 80$. Approximately $400\times\ 10^6$ grid points are used for the simulations. A three-dimensional domain decomposition method is used to distribute the sub-domains into 96 and 192 processors for the auxiliary and main simulations, respectively. Exchange of the data between the processors is performed through the message passing interface (MPI) library. The main simulations required approximately 20 000 CPU h on a Cray XE6.

Note that a temporal simulation is additionally performed to compare with its spatial counterpart, SP50. The dimensions of the computational domain and the mesh size for this simulation are the same as that of the auxiliary simulation for the generation of the inflow boundary condition.

III. DATA ANALYSIS METHOD

Since we are computing a spatially evolving stratified wake, we have inhomogeneous boundaries in every direction. Therefore, spatial averaging of the variables in a particular direction, as can be done for temporally evolving simulations, is infeasible. We perform temporal averaging of the variables for calculating the statistics. The simulations are run for a sufficiently long time($1.5L_1/U_\infty$) to reach a statistically homogeneous state for performing a temporal averaging as follows:

$$\langle \phi(x_1, x_2, x_3) \rangle = \frac{1}{T_2 - T_1} \int_{T_1}^{T_2} \phi(x_1, x_2, x_3, t) dt, \tag{14}$$

where the angle brackets represent temporal averaging, T_1 is the start and T_2 is end of time averaging and $T_2 - T_1$ is $\sim 0.8L_1/U_\infty$. The Reynolds decomposition of the flow variables is

$$u_i = \langle u \rangle + u_i', \quad \rho = \langle \rho \rangle + \rho', \quad p = \langle p \rangle + p'. \tag{15}$$

The integrated turbulent kinetic energy, $TKE = \int_A \langle u_i' u_i' \rangle / 2 dA$, is a measure of the kinetic energy of the fluctuations. The evolution of the pointwise turbulent kinetic energy, $K = \langle u_i' u_i' \rangle / 2$ is given by

$$\frac{DK}{Dt} = P + B - \varepsilon - \frac{\partial T_i}{\partial x_i}, \tag{16}$$

where P is the production is given by

$$P = -\langle u_i' u_j' \rangle \frac{\partial \langle u_i \rangle}{\partial x_j}, \tag{17}$$

ε is the turbulent dissipation rate given by

$$\varepsilon = \frac{2}{Re} \langle s_{ij}' s_{ij}' \rangle, \qquad s_{ij}' = \frac{1}{2} \left(\frac{\partial u_i'}{\partial x_j} + \frac{\partial u_j'}{\partial x_i} \right). \tag{18}$$

Here, $\partial T_i / \partial x_i$ is the turbulent transport and is defined as

$$T_i = \frac{1}{2} \langle u_i' u_j' u_j' \rangle - \langle u_i' p' \rangle - \frac{2}{Re} \langle u_j' s_{ij}' \rangle, \tag{19}$$

while B, the buoyancy flux that transfers energy between the turbulent kinetic and potential energy modes, is given by

$$B = -\frac{1}{Fr^2} \langle \rho' u_3' \rangle. \tag{20}$$

For the comparison of the wake dimensions, we calculate the wake thickness in the horizontal and vertical based on the wake kinetic energy. The horizontal thickness, R_{E2} is obtained by fitting a Gaussian profile to the horizontal variation of KE and computing its width at 1% of the maximum, centerline value. The variation in the vertical is more complex with auxiliary off center lobes and, therefore, the vertical thickness is calculated by using a second central spatial moment of the KE in the vertical direction as done by Brucker and Sarkar,[14]

$$R_{X\alpha}^2 = A_1 \frac{\int_A (x_\alpha - x_\alpha^c)^2 (X) dA}{\int_A (X) dA}. \tag{21}$$

Here, $x_\alpha^c(t) = \frac{\int_A (x_\alpha)(X) dA}{\int_A (X) dA}$, $A_1 = 2$ is a normalization factor to set the initial wake dimensions, A is the area of the $x_2 - x_3$ plane excluding the sponge region and $\alpha = 3$. The choice of $X = \langle u_i \rangle \langle u_i \rangle / 2 + \langle u_i' u_i' \rangle / 2$ corresponds to spatial extent of wake kinetic energy.

The energy flux radiated to the background by internal waves is given by

$$T_p = \int_C \langle p' u_n' \rangle dC, \tag{22}$$

where C denotes the closed curve corresponding to the $x_2 - x_3$ plane excluding the sponge region and u_n' is the velocity fluctuation in the direction normal to the boundary.

IV. SUMMARY OF A SPATIALLY EVOLVING SELF-PROPELLED WAKE

As mentioned in Sec. II, we perform a spatial simulation of a stratified wake with specified turbulent inflow conditions. The stratified wake consists of various flow regimes whose duration is typically given in terms of buoyancy period, Nt. The period $Nt < 2$ is the NW region where the wake evolves as an unstratified flow. The regime $2 < Nt \approx 50$ is the NEQ, which is further split into an accelerated collapse (AC) region, $2 < Nt < 7$, and a transition region, $7 < Nt \approx 50$. The $Nt > 50$ regime is referred to as the $Q2D$ stage of the late wake. In the NW regime, the wake expands in both x_2 and x_3 directions mixing up the background density field by displacing heavy fluid up and

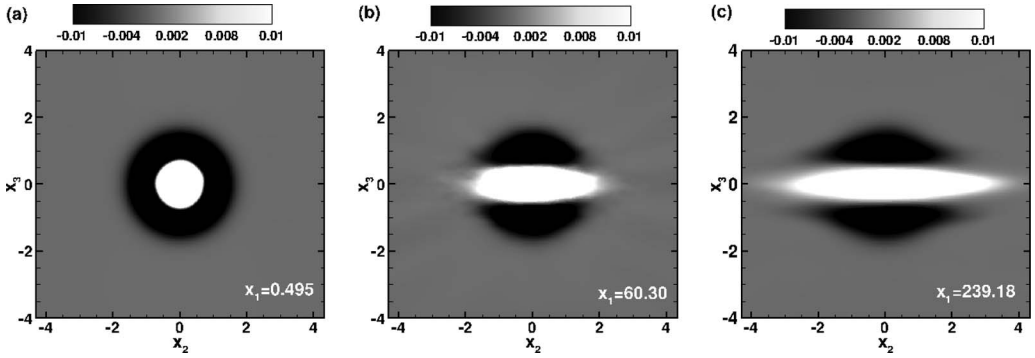

FIG. 2. Mean velocity contours for self propelled wake (SP50) at various x_1 locations. Case SP50.

light fluid down. When the wake enters the *AC* regime, the stabilizing effect of buoyancy becomes significant and the kinetic energy is sustained at the expense of the potential energy. The density perturbations are no longer supported by the kinetic energy, due to which the fluid seeks equilibrium and the flow is suppressed in the vertical direction whereas in the lateral direction, the wake expands. This effect also slows down the decay of the horizontal mean velocity and radiates energy in the form of internal gravity waves into the background. Figure 2 illustrates the contours of the evolution of the mean velocity $\langle u_1 \rangle(x_2, x_3)$ at various x_1 locations. Figure 2(a) shows the initial mean velocity profile with the presence of initially axisymmetric positive velocity lobes (thrust lobes) and negative velocity lobes (drag lobes) whereas Figures 2(b) and 2(c) depict the subsequent anisotropic growth of the wake that occurs primarily in the horizontal direction. The negative velocity lobes eventually vanish in the horizontal direction but remain in the vertical direction over the entire downstream extent. The reason for the survival of the negative lobes is the effect of buoyancy that inhibits vertical mixing of momentum.

Internal gravity waves carry horizontal vorticity. The wave field associated with the self-propelled wake is shown via the contours of ω_1 in Figure 3 at various downstream locations. In addition, Figure 3(d) shows that, at late time, the central region of the wake has multiple coherent layers of streamwise vorticity. These correspond to regions of large vertical shear between adjacent pancake eddies.

Figure 4 shows the instantaneous vertical vorticity field at the centerplane in the horizontal direction. Small vortices merge to form large vortices in the downstream directions. These vortices ultimately take the form of coherent pancake eddies as shown in earlier laboratory experiments and temporally evolving simulations. The frequency spectra at various downstream locations are shown in Figure 5. Kolmogorov scaling (ω^{-2}) is found over a short range of wavenumbers at the locations $x_1 = 2.25$, 47.36, and 98.91; however, spectra at locations further downstream with lower turbulent Reynolds number exhibit a decay faster than ω^{-2}.

Figures 6(a) and 6(b) show Reynolds stresses, $\langle u_1' u_2' \rangle$ and $\langle u_1' u_3' \rangle$, respectively, at the location $x_1 = 75.18$. The horizontal fluctuations have a Reynolds stress, $\langle u_1' u_2' \rangle$, that is antisymmetric and with a sign (positive/negative) consistent with co-gradient turbulent transport by the mean velocity. However, $\langle u_1' u_3' \rangle$ shows little coherence with the mean field. The spatial evolution of $\langle u_1' u_3' \rangle$ also exhibits a rapid decrease followed by oscillation around a value of zero. The faster decay of $\langle u_1' u_3' \rangle$ relative to $\langle u_1' u_2' \rangle$ occurs because buoyancy inhibits the magnitude of vertical fluctuations as well as their correlation with horizontal fluctuations, whereas the mean velocity shear in the horizontal plane is able to maintain $\langle u_1' u_2' \rangle$ that is associated with fluctuations that are not directly affected by buoyancy. This behavior of the Reynolds shear stresses is similar to that found by Jacobitz and Sarkar[29] in uniform shear flow who examined the effect of changing the inclination of mean shear plane so that the ratio of vertical mean shear to horizontal mean shear progressively changed from unity to zero. However, there is an important difference with the previously studied situation with uniform shear. The follow up study of Jacobitz and Sarkar[30] found that the growth rate of the turbulent kinetic energy in the case of horizontal mean shear decreased with increasing

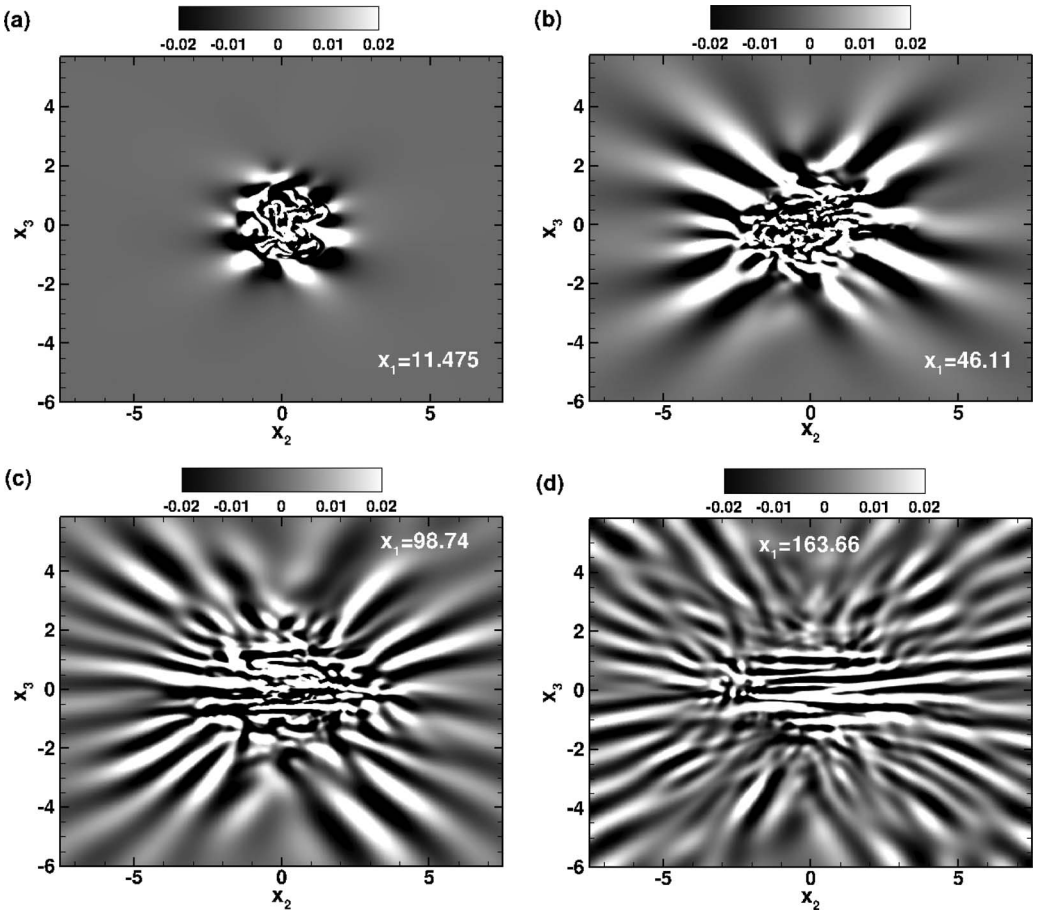

FIG. 3. Internal gravity wave field visualized by snapshots of ω_1 at various x_1 locations. Multiple horizontal layers, a manifestation of the dislocations between pancake eddies, can also be seen in (d). Case SP50.

gradient Richardson number, Ri, as in vertically sheared flow until, at a critical Richardson number $Ri_{cr} \sim 1.5$, the kinetic energy of fluctuations asymptotically decayed to zero instead of growing. In contrast, the inflectional nature of the mean horizontal shear in the present case of a wake ensures that shear instabilities continually maintain velocity fluctuations.

A. Comparison between a spatially and a temporally evolving self-propelled wake

The validity of the temporally evolving approximation given an initial field corresponding to a spatially evolving model is of interest. Therefore, we simulate the SP50 case with a temporally evolving model and compare the various statistics from the two simulations in Figure 7. Results for the temporal simulation are plotted as a function of time, t, and for the spatial simulation as a function of x_1. The simulations have a virtual origin of $t = 7$ and $x_1 = 7$, based approximately on measured turbulence levels in wakes. The wave flux and the integrated production (Figures 7(c) and 7(d), respectively) between the spatial and temporal simulations are similar. Although there is similarity in the behavior of the integrated dissipation (Figure 7(d)) between both types of simulations, there are some differences which could be due to the somewhat higher grid spacing (owing to grid stretching) in the spatial simulation. Figure 7(e) shows that the buoyancy flux is similar between the temporal and spatial models. We also observe a similar distribution of waves and vortical structures (not shown) in contour plots.

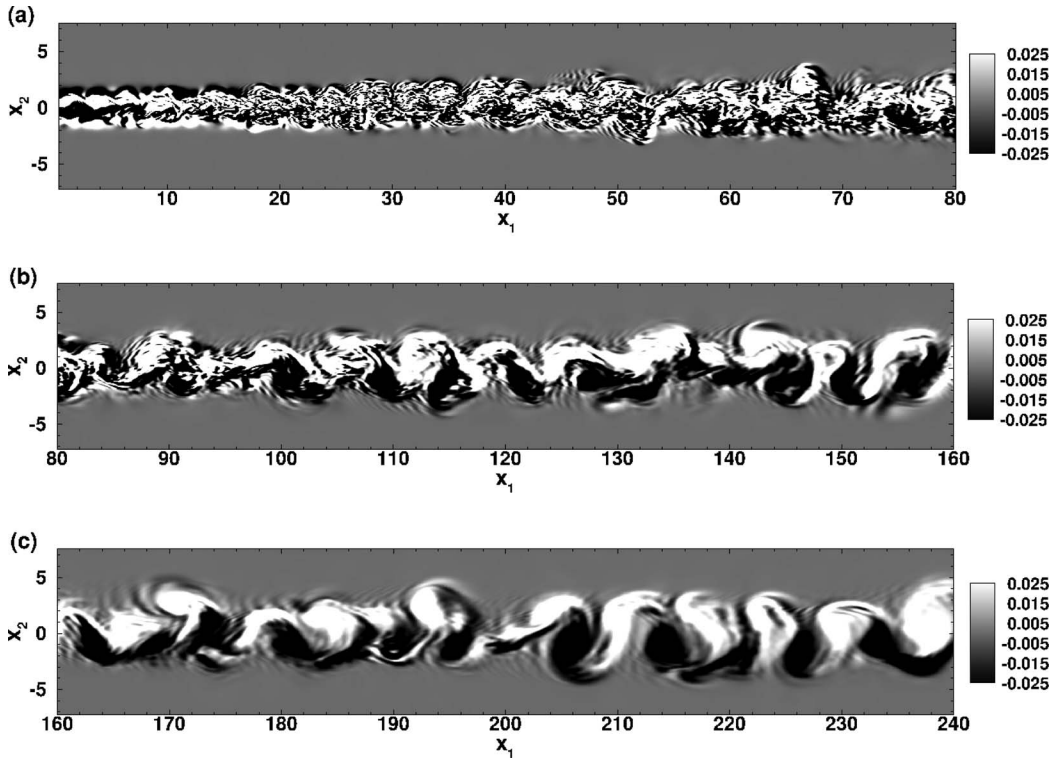

FIG. 4. Instantaneous ω_3 at the horizontal centerplane, $x_3 = 0$ (a) $0 < x_1 < 80$, (b) $80 < x_1 < 160$, and (c) $160 < x_1 < 240$. Case SP50.

V. COMPARISON BETWEEN A SPATIALLY EVOLVING SELF-PROPELLED WAKE AND A PATCH OF TURBULENCE

The initial energy spectra used for the simulations of a self-propelled wake with 50% mean kinetic energy (*MKE*) and the turbulent patches were shown in Figure 1(b). Comparison between case SP50 (with mean shear) and case TP1 (without mean shear but with inlet turbulence similar to SP50) allows us to make precise the role of mean shear in the flow evolution while comparison

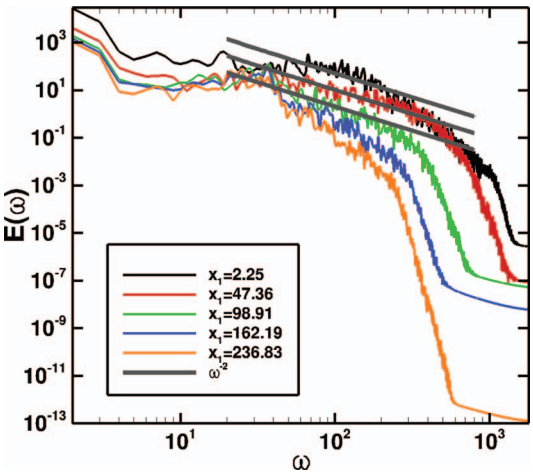

FIG. 5. Frequency spectra at various downstream locations. Case SP50.

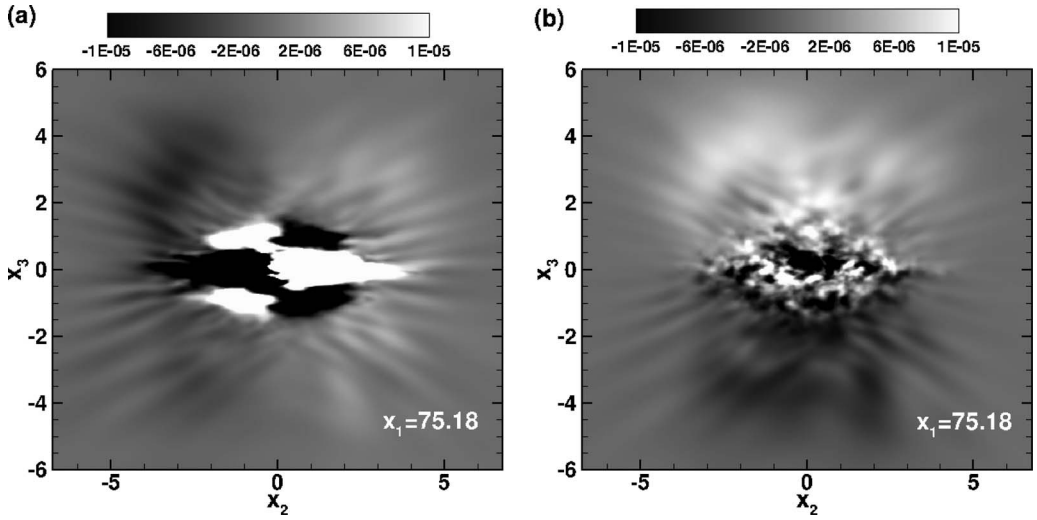

FIG. 6. Reynolds stresses (a) $\langle u_1' u_2' \rangle$ and (b) $\langle u_1' u_3' \rangle$. Case SP50.

between cases TP1 and TP2 (different energy spectrum with more small-scale contribution) allows us to explore the influence of initial fluctuations in the near wake.

Figure 8 shows the evolution of the integrated *TKE* normalized by its inlet value for different cases. It can be observed that the integrated *TKE* of SP50 exhibits an initial decay that is small relative to TP1 and TP2. This difference occurs because of the presence of shear production of *TKE* in case SP50 that extracts energy from the mean and transfers it into the fluctuations. The production not only restrains the *TKE* from decaying during the initial stages but increases it until $x_1 \sim 18$. As the production starts decreasing, the extraction of energy from the mean decreases and the *TKE* in case SP50 also starts decaying. Note that the shear production is identically zero in the TP cases. The decay of *TKE* in cases SP10 and TP10 (they are the analogous cases to SP50 and TP1, i.e., SP10 has 10% *MKE* and TP10 has the same initial spectrum as SP10) as shown in Figure 8 is found to be almost similar in contrast to the differences between SP50 and TP1. The reason for the similar decay of *TKE* between cases SP10 and TP10 is the small percentage of *MKE* in SP10, which leads to a smaller production than in SP50 and, therefore, a smaller counter to dissipative effects on *TKE*.

After the slight initial decay of *TKE* in SP50, it increases up to a peak value and starts decaying again as seen in Figure 8. We see an increase in integrated *TKE* as well for TP1 but the increase is not as large as SP50. This increase of the *TKE* in case TP1 is due to the buoyancy flux being positive at this time as shown in Figure 10(b). The *TKE* in case TP2 decays in a similar manner as in TP1 up to $x_1 \sim 11$, but instead of an increase at $x_1 \sim 11$ the TKE decays at a slower rate because of the positive buoyancy flux.

Figure 9(a) shows the evolution of integrated production (already discussed) and integrated dissipation. Case TP2 has larger turbulent dissipation rate relative to SP50 and TP1 because of the higher small-scale energy content. Going downstream, the turbulent dissipation for SP50 increases, increases slightly for TP1, and decreases for TP2. The increase in the dissipation of SP50 is due to the transfer of energy from the mean shear into the fluctuating components. The dissipation increases until $x_1 \sim 20$, as the production and buoyancy flux achieves a second peak value at the same location. For $x_1 > 20$ both the production and dissipation decrease in case SP50. The components of integrated production, P_{12} and P_{13}, are shown in Figure 9(b). P_{12} decreases monotonically but remains positive whereas P_{13} decreases and becomes negative at $x_1 \sim 16$. For $x_1 > 16$, P_{13} increases to a positive value and then decreases again to a negligible value. Recall that the mean velocity contours of Figure 2 shows that the initial lobes of negative velocity disappeared in the horizontal axis but were maintained in the vertical axis. The reason is that P_{12} (always positive) is able to continuously extract energy from the mean shear to fluctuations and continuously reduce the mean shear in the horizontal x_2 direction. P_{13}, on the other hand, extracts energy from the vertical mean shear initially but then

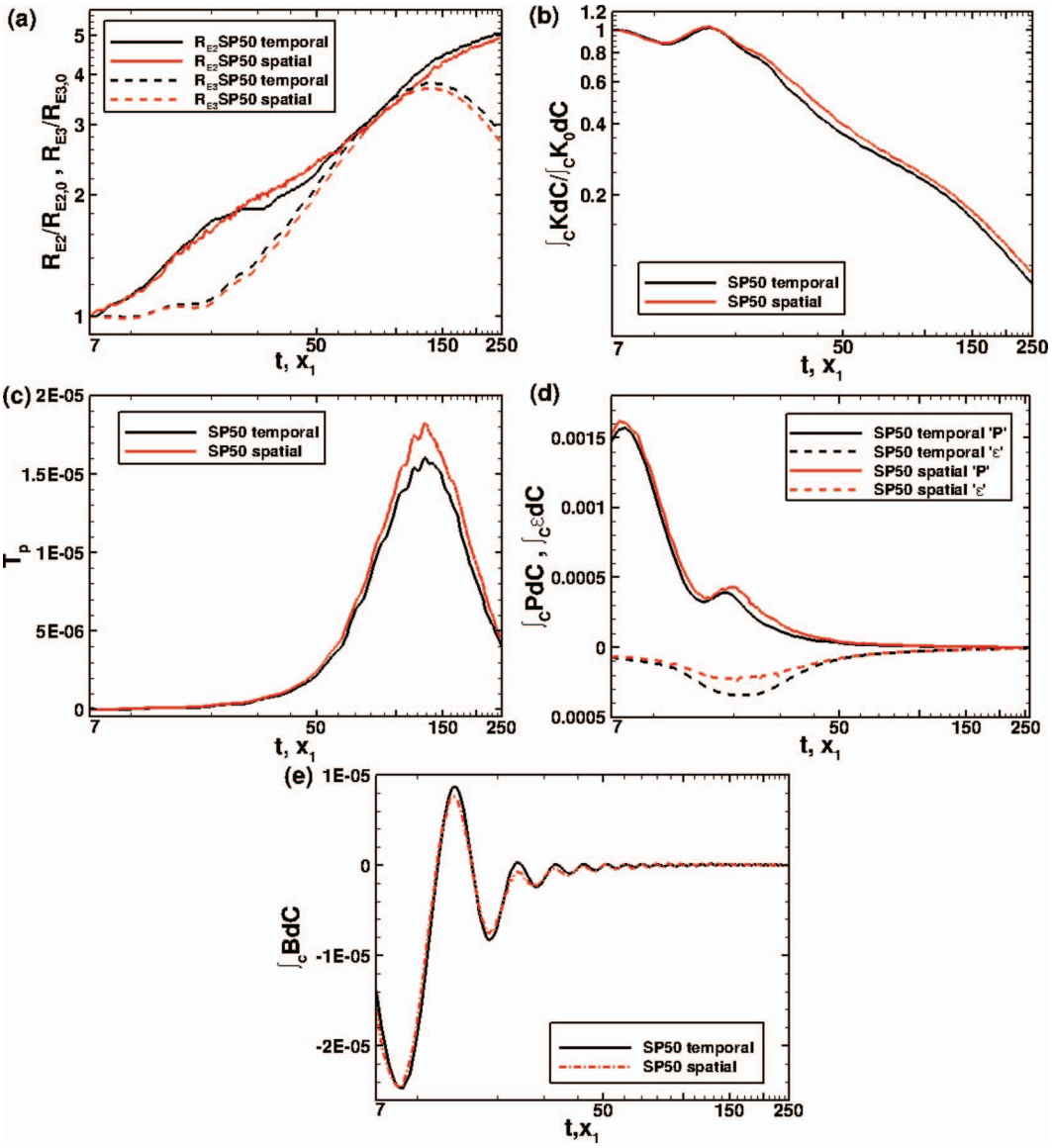

FIG. 7. Comparison between temporal and spatial simulations: (a) wake dimensions, (b) integrated turbulent kinetic energy, (c) wave flux, (d) integrated production and dissipation, and (e) integrated buoyancy flux.

returns a part of the extracted energy to the mean, and eventually oscillates between positive and negative values with little mixing of momentum. At the end there is a residual of mean energy thus maintaining the negative lobes in the vertical profile of mean velocity.

Figures 10(a) and 10(b) show the x_1 and x_3 component of the integrated *TKE* and the integrated buoyancy flux, respectively. There is oscillatory behavior of integrated K_{33} and buoyancy flux in all the cases owing to the reversible exchange between potential and kinetic energy in stratified flow. We also find from Figure 10(a) that K_{11} increases for SP50 in the near wake and decays at downstream locations whereas for TP1 and TP2 it decreases monotonically from the initial value. The rate of decay of K_{11} in case TP2 is steeper than for TP1. K_{22} (not shown here) behaves identically as K_{11} for TP1 and TP2, but for SP50 it shows a smaller increase at initial stages and slower rate of decay at later stages as compared to K_{11}. The oscillations in the vertical component, K_{33}, lead to an increase in the integrated *TKE* of SP50 and TP1 in the initial stages as was evident from Figure 8(b). Figure 10(a) shows that K_{33} decreases by almost 50% before it regains the initial value at $x_1 \sim 18$.

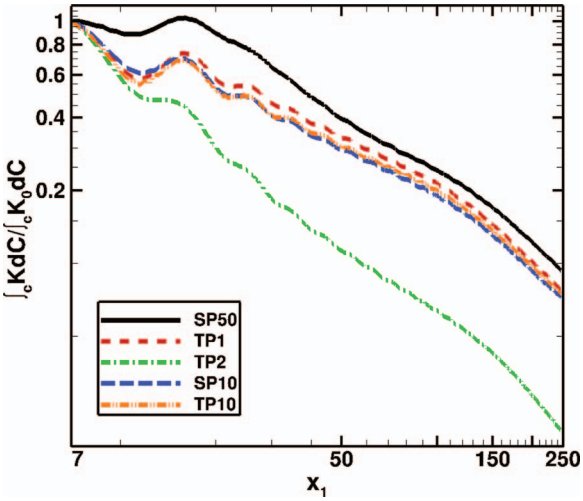

FIG. 8. Integrated turbulent kinetic energy SP50, TP1, TP2, SP10, and TP10.

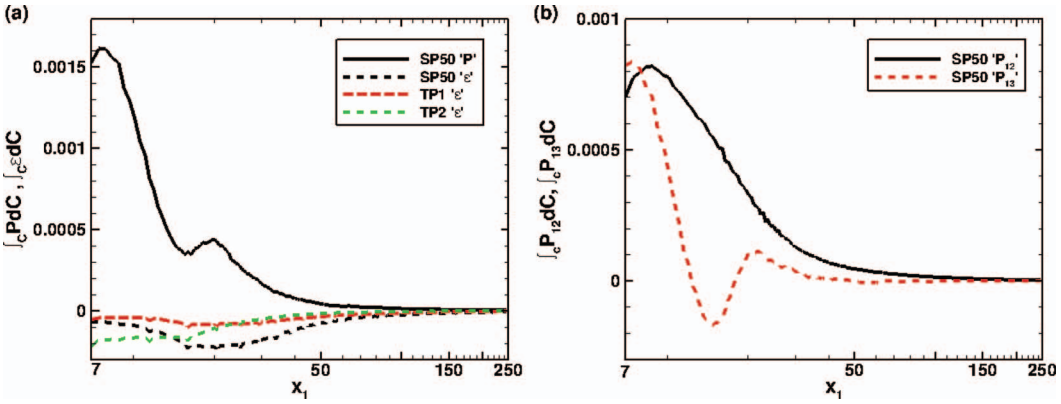

FIG. 9. (a) Production and dissipation integrated over the cross-section area. Note that production is identically zero for TP1 and TP2. (b) Components of production integrated over the cross-section area.

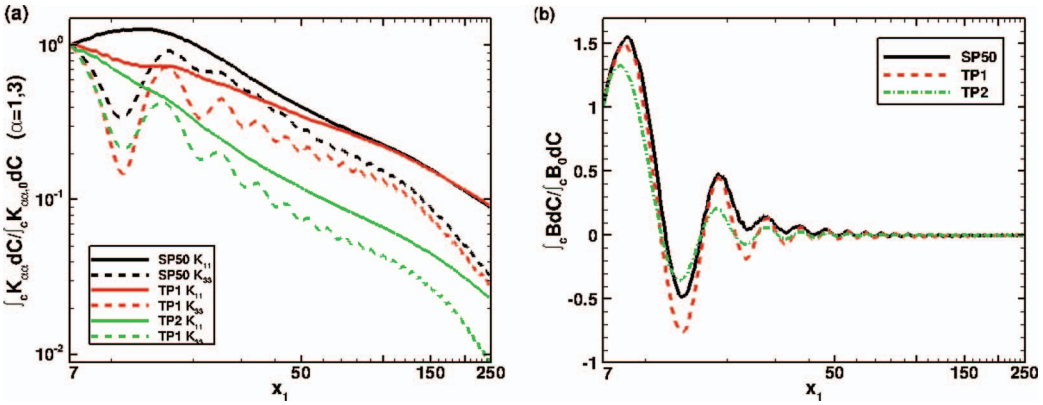

FIG. 10. (a) x_1 and x_3 components of integrated *TKE* and (b) integrated buoyancy flux.

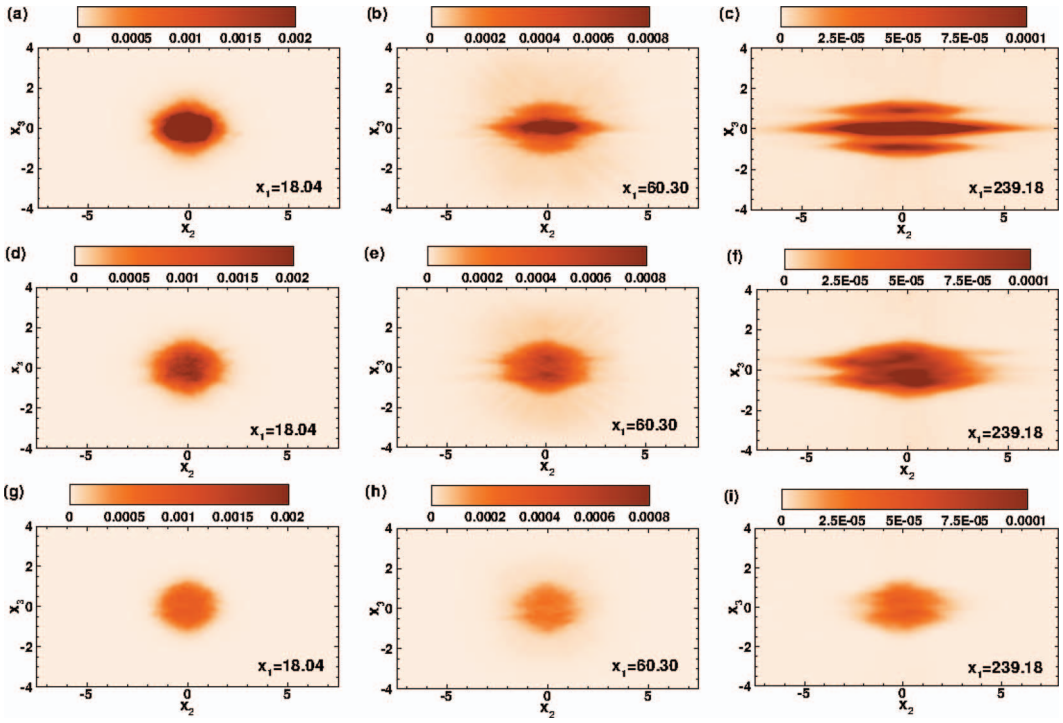

FIG. 11. Evolution of *TKE* contours with the evolution of each case shown as a horizontal row. The top row (parts (a)–(c)) correspond to the self-propelled wake with 50% mean (SP50), the middle row ((d)–(f)) to TP1, and the bottom row ((g)–(i)) to TP2.

This is supported by the large values of the integrated buoyancy flux in the near wake as shown in Figure 10(b).

Figure 11 shows contours of the *TKE* of the self-propelled wake with 50% mean and the two patch-of-turbulence cases with different spectra at various x_1 locations. At $x_1 \simeq 18$, the distribution of *TKE* is already different among cases. The shear production transfers energy into the fluctuating components of velocity in case SP50 and, therefore, we see a higher concentration of *TKE* in the core of the SP50 case (Figure 11(a)) as compared to TP1 and TP2 (Figures 11(d) and 11(g)). The difference in the *TKE* between cases TP1 and TP2 is due to the higher initial dissipation rate of TP2. As we move downstream, the *TKE* in SP50 expands preferentially in the horizontal direction because of entrainment that is not directly inhibited by buoyancy. *TKE* in case TP1 decays in a manner that is qualitatively similar to SP50 whereas in case TP2 the *TKE* decays much faster.

This can again be related to the fact that the dissipation of TP2 is higher than SP50 and TP1 initially and there is no energy transfer into the fluctuations because of the lack of mean shear. The distinctive feature of SP50 relative to TP1 and TP2 is the presence of lobes in the vertical direction as shown in Figures 11(c), 11(f), and 11(i). The presence of lobes can be explained in a similar manner as done earlier for the presence of the negative lobes in the mean velocity profile. The reversible energy transfer by P_{13} leaves fluctuating energy lobes in the vertical direction as residual.

The evolution of internal wave flux is shown in Figure 12. We notice that SP50 shows a higher wave flux as compared to TP1, whereas TP2 has a substantially smaller wave flux amongst all of the cases. This happens due to the fact that the flow in case SP50 inherits more *TKE* than TP1 which in turn has higher *TKE* than TP2 as depicted in Figure 8(a). The higher the fluctuation energy in the core of the wake, the higher will be the energy propagated into the background during the suppression of the wake growth in the vertical direction. Furthermore, TP2 has less energy in the low-wave numbers that drive the wave flux. SP10 and TP10 show similarity in the evolution of wave flux. Higher values of *TKE* in SP50 lead to higher wave flux as compared to SP10.

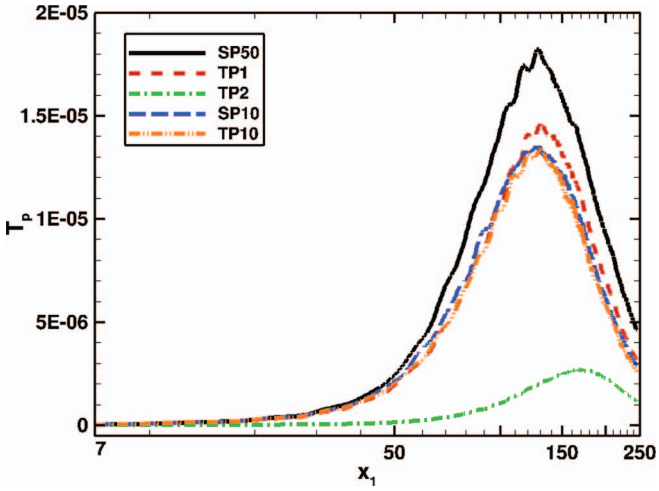

FIG. 12. Internal wave flux for SP50, TP1, TP2, SP10, and TP10.

Figures 13(a) and 13(b) represent the evolution of wake dimensions in the horizontal and the vertical directions calculated using the total kinetic energy. The variation in the lateral direction is well-fitted by a Gaussian profile whose radius, R_{E2}, is computed based on the 1% of maximum, centerline value. The variation of kinetic energy in the vertical direction exhibits auxiliary peaks on each side in addition to the central peak. Therefore, the vertical radius, R_{E3}, is calculated using Eq. (21), an expression based on the second central moment of the kinetic energy. The horizontal wake thickness expands at different rates that decreases from SP50 to TP1 to TP2. Similarly, the horizontal wake thickness is lower in TP10 relative to SP10. At further downstream locations, the expansion of case TP2 in the horizontal direction is very small relative to the other cases. A possible reason is that the coherence of the vertically oriented late-wake vortices is much less in TP1 as will be shown shortly. The vertical thickness, R_{E3}, does not increase initially because buoyancy suppresses turbulent entrainment. After $x_1 \sim 30$, the vertical thickness exhibits an increase in cases SP50 and TP1 up to $x_1 \sim 130$ and until $x_1 \sim 180$ in case TP2. All cases show an eventual contraction in the vertical thickness, an unusual occurrence in turbulent flows. The increase in R_{E3} occurs due to fluctuation energy being deposited in the regions adjacent to the wake core by the internal wave flux. But, eventually the wave flux decreases leading to the downstream decrease in R_{E3}. We note that the increase and subsequent decrease of R_{E3} occurs because of the choice of KE (dominated by

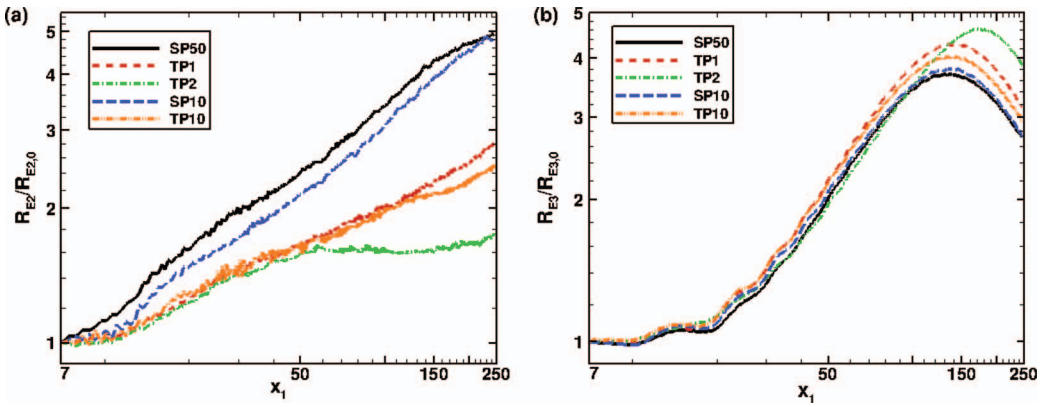

FIG. 13. Wake dimensions based on the kinetic energy for SP50, TP1, TP2, SP10, and TP10: (a) wake width and (b) wake height.

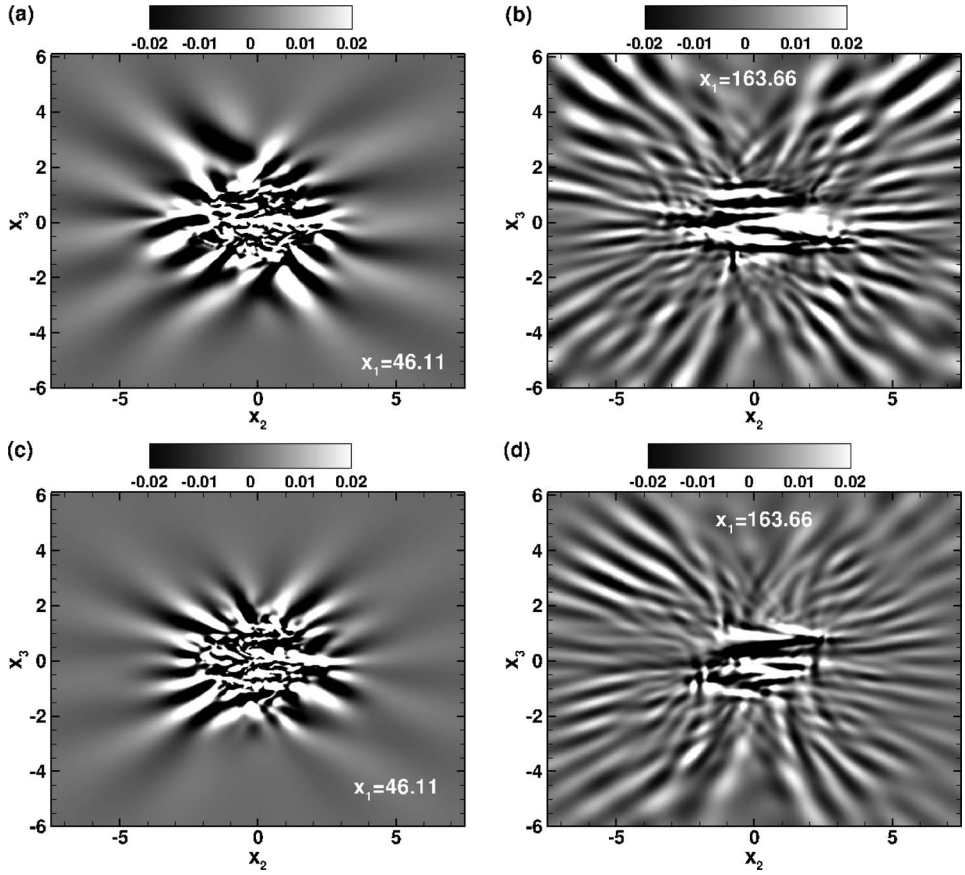

FIG. 14. Internal gravity wave field visualized by contours of ω_1 at various x_1 locations for cases TP1 (upper row) and TP2 (lower row).

fluctuation KE) to evaluate the vertical extent of the wake. For instance, R_3 in the wake (case SP50) based on the mean velocity shows little increase in the downstream direction.

The spatial structure of the internal wave field is similar between the two turbulent patch cases shown in Figure 14 and similar to that for the SP50 case that was shown earlier in Figure 3. One difference is that the magnitude of ω_1 outside the core of the wake is smaller in TP2, consistent with the smaller wave flux T_p. The organization of the streamwise vorticity into coherent horizontal layers spanning the wake width that was seen earlier in SP50 is seen in the turbulent patches too.

The vertical vorticity in the late wake region of case SP50 exhibited large coherent vortex dipoles as was shown in Figure 4. Figure 15 shows that the vertical vorticity is less organized in the turbulent patches without mean shear. Especially, in case TP2, the vortical structures are much smaller and do not show clear vortex dipoles. Evidently, the initial presence of a larger fraction of fluctuation energy of TP2 in smaller length scales further inhibits the coherence of the vortices. At much later time, $t > 400$, larger coherent vortices do emerge in cases TP1 and TP2, but they are significantly weaker than the vortices at corresponding time in the wake with mean shear.

VI. EFFECT OF INITIAL ENERGY SPECTRUM ON THE WAKE EVOLUTION

In order to evaluate the effect of the initial spectrum on the evolution of the wake, we compare temporal simulations of cases SP50 and SP50C. Both cases have the same initial TKE but SP50C has higher energy at smaller scales, similar to TP2, as shown in Figure 1(b). The simulation parameters for SP50C are given in Table I. Figures 16(a)–16(d) show a comparison of various statistics between

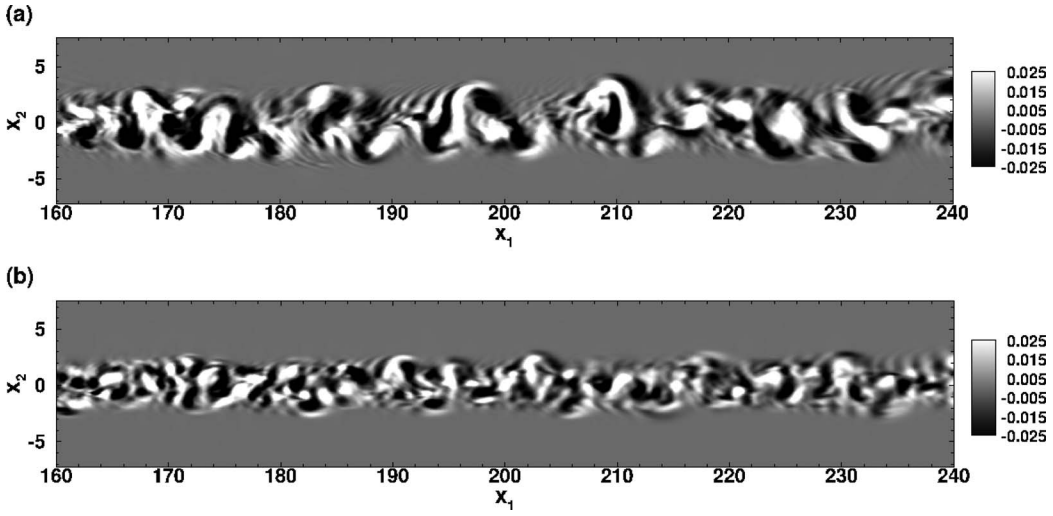

FIG. 15. Vertical vorticity shown far downstream ($160 < x_1 < 240$) in the turbulent patch simulations: (a) turbulent patch TP1 and (b) turbulent patch TP2. Instantaneous ω_3 at the horizontal centerplane is shown for both cases.

SP50 and SP50C. In Figure 16(a), we find that the integrated turbulent kinetic energy decays faster in case SP50C as compared to SP50 because of the higher integrated turbulent dissipation in Figure 16(b), consistent with the higher initial fluctuation energy at the small scales (Figure 1(b)) in SP50C. The values of the integrated production are similar between the two cases. The MKE plotted in Figure 16(c) is similar in the two cases except for a somewhat smaller value in SP50 relative

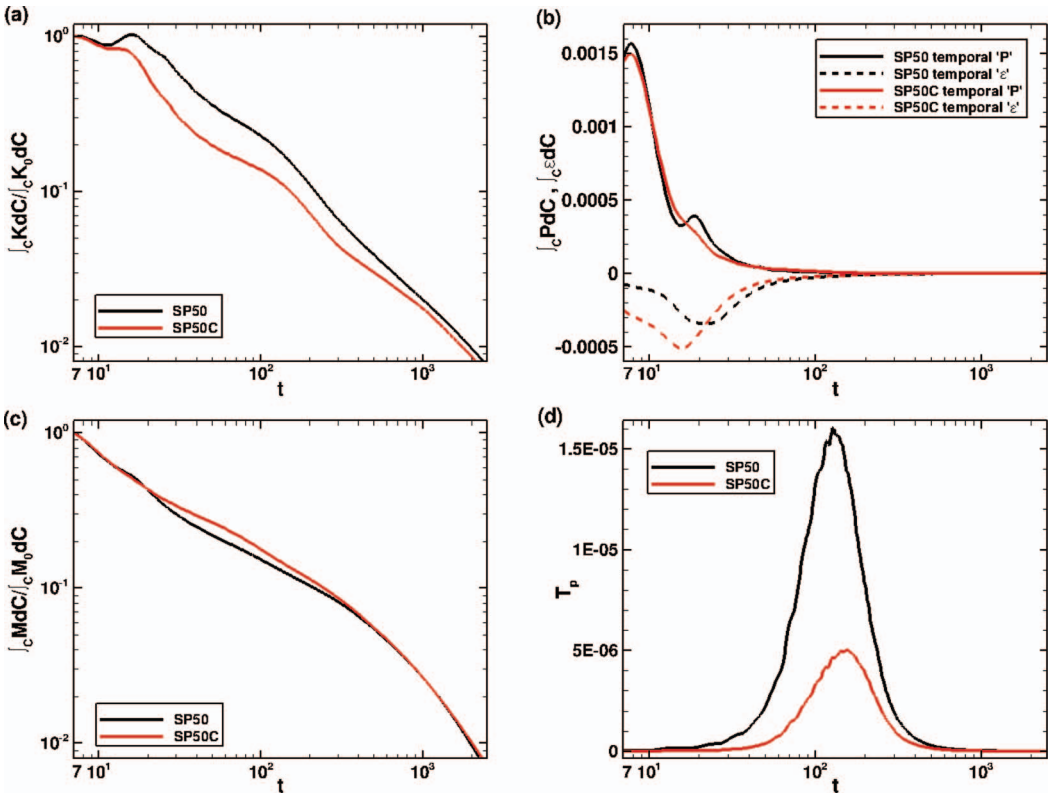

FIG. 16. Comparison between SP50 and SP50C: (a) integrated turbulent kinetic energy, (b) integrated production and dissipation, (c) integrated MKE, and (d) wave flux.

to SP50C during $20 < t < 200$. During this time period, the internal wave flux is larger in SP50 as shown in Figure 16(d) and, consistent with the stronger waves, the wave transport $\langle u'w' \rangle \langle U \rangle$, is larger in case SP50 leading to lower mean velocity and lower MKE. It is worth noting that the larger internal wave flux in case SP50 is consistent with higher fluctuation energy, relative to SP50C, in Figure 16(a).

Similar to TP2, case SP50C was initiated with the fluctuation energy distributed preferentially at smaller scales relative to case SP50 and TP1. Different from TP2, case SP50C has an initial mean velocity profile that influences the large scales of the fluctuating energy through horizontal instabilities. Consequently, there is a major difference with respect to TP2: case SP50C exhibits large coherent structures of vertical vorticity that are similar to those in SP50, shown previously in Figure 4, and the horizontal extent of the wake in SP50C also evolves similarly so as to reach values that are substantially larger than in case TP2.

VII. DISCUSSION AND CONCLUSIONS

DNS of a spatially evolving self-propelled wake with zero integrated momentum and a patch of turbulence has been performed at $\mathrm{Re} = 15\,000$ in a stratified fluid to examine the influence of the canonical self-propelled mean velocity profile on the evolution of the wake. The mean velocity affects the evolution of the wake depending upon the amount of mean kinetic energy present in the wake. If the mean kinetic energy is of the order of 10% of the total kinetic energy, the wake evolves similarly to a patch of turbulence with the *same* initial energy spectrum of the fluctuations. But if the mean kinetic energy is increased to 50% in case SP50 we find significant differences in the turbulence statistics for the near to early intermediate wake, moderate differences for the intermediate wake and minor difference for the late wake with respect to a patch of turbulence, TP1. Both the wake and turbulent patch show similar spatial features in the internal wave field but the dipole pattern of the late-wake vortices is more evident in the wake relative to the turbulent patch. Strongly stratified flows are known to exhibit vertical layering of the vorticity field. Such layering is found in both the wake and the turbulent patch.

The spectral content of the near wake can differ between cases owing to factors such as different boundary layer characteristics. The influence of spectral distribution of fluctuation energy is studied here by simulating a turbulent patch case, TP2, that has substantially higher energy content at smaller length scales compared to case TP1 although the initial rms fluctuations are the same. Case TP2 with higher small-scale energy exhibits changes in its evolution relative to case TP1: the *TKE* is significantly smaller during the evolution, the internal wave radiation is weaker, and the late-wake vortices are smaller and less coherent. In order to evaluate the effect of initial energy spectrum on the wake evolution, case SP50C with the same initial *TKE* as SP50 but higher small-scale energy content was simulated. Relative to SP50, the evolution of case SP50C exhibits significantly smaller *TKE*, weaker internal wave flux consistent with the difference that TP2 has with respect to TP1. However, large coherent structures that were seen to form in case SP50 also form in case SP50C and, similar to case SP50, the stratified wake of SP50C also has a substantially larger horizontal extent than the turbulent patches. Evidently, the presence of mean horizontal shear influences the low-wave number part of the energy spectrum resulting in large coherent vortices with enhanced horizontal entrainment.

Another objective of the present DNS study of stratified wakes was to compare the accuracy of the temporally evolving approximation that is often made because of the considerable savings in computational cost. We find that the temporal approximation, when provided with initial conditions that match the inflow conditions of a spatially evolving computational model, leads to mean and turbulent statistics that agree well with those in the spatially evolving flow. The reason is that the approximation of linearizing the nonlinear advection term in the averaged equations around uniform flow is small in the case of a wake since the wake deficit velocity is small compared to the uniform flow. Even when the initial value of the mean kinetic energy in the wake is as large as 50% of the total (mean plus fluctuation), its relative contribution decreases rapidly ensuring the validity of the temporal approximation.

ACKNOWLEDGMENTS

We are grateful to acknowledge the support of ONR Grant No. N0014-11-10469 administered by Dr. Ron Joslin. Computational resources were provided by the Department of Defense High Performance Computing Modernization Program. We would also like to thank the two anonymous referees whose helpful suggestions improved the quality of this paper.

[1] J. T. Lin and Y. H. Pao, "Wakes in stratified fluids," Annu. Rev. Fluid Mech. **11**, 317–338 (1979).
[2] E. Naudascher, "Flow in the wake of self-propelled bodies and related sources of turbulence," J. Fluid Mech. **22**(4), 625–656 (1965).
[3] H. Higuchi and T. Kubota, "Axisymmetric wakes behind a slender body including zero-momentum configurations," Phys. Fluids **2**(9), 1615–1623 (1990).
[4] A. I. Sirviente and V. C. Patel, "Wake of a self-propelled body, Part 1: Momentumless wake," AIAA J. **38**(4), 613–619 (2000).
[5] J. M. Chomaz, P. Bonneton, and E. J. Hopfinger, "The structure of the near wake of a sphere moving horizontally in a stratified fluid," J. Fluid Mech. **254**, 1–21 (1993).
[6] J. M. Chomaz, P. Bonneton, A. Butet, and E. J. Hopfinger, "Vertical diffusion of the far wake of a sphere moving horizontally in a stratified fluid," Phys. Fluids **5**, 2799–2806 (1993).
[7] G. R. Spedding, F. K. Browand, and A. M. Fincham, "Turbulence, similarity scaling and vortex geometry in the wake of a towed sphere in a stably stratified fluid," J. Fluid Mech. **314**, 53–103 (1996).
[8] G. R. Spedding, "The evolution of initially turbulent bluff-body wakes at high internal Froude number," J. Fluid Mech. **337**, 283–301 (1997).
[9] G. R. Spedding, "Vertical structure in stratified wakes with high initial Froude number," J. Fluid Mech. **454**, 71–112 (2002).
[10] M. J. Gourlay, S. C. Arendt, D. C. Fritts, and J. Werne, "Numerical modeling of initially turbulent wakes with net momentum," Phys. Fluids **13**, 3783–3802 (2001).
[11] D. G. Dommermuth, J. W. Rottman, G. E. Innis, and E. A. Novikov, "Numerical simulation of the wake of a towed sphere in a weakly stratified fluid," J. Fluid Mech. **473**, 83–101 (2002).
[12] J. J. Riley and S. M. de Bruyn Kops, "Dynamics of turbulence strongly influenced by buoyancy," Phys. Fluids **15**(7), 2047–2059 (2003).
[13] G. Brethouwer, P. Billant, E. Lindborg, and J. M. Chomaz, "Scaling analysis and simulation of strongly stratified turbulent flow," J. Fluid Mech. **585**, 343–368 (2007).
[14] K. A. Brucker and S. Sarkar, "A comparative study of self-propelled and towed wakes in a stratified fluid," J. Fluid Mech. **652**, 373–404 (2010).
[15] P. Meunier, P. J. Diamessis, and G. R. Spedding, "Self-preservation in stratified momentum wakes," Phys. Fluids **18**(10), 106601 (2006).
[16] P. J. Diamessis, G. R. Spedding, and J. A. Domaradzki, "Similarity scaling and vorticity structure in high Reynolds number stably stratified turbulent wakes," J. Fluid Mech. **671**, 52–95 (2011).
[17] A. M. Abdilghanie and P. J. Diamessis, "The internal gravity wave field emitted by a stably stratified turbulent wake," J. Fluid Mech. **720**, 104–139 (2013).
[18] B. R. Sutherland and P. F. Linden, "Internal wave excitation from stratified flow over a thin barrier," J. Fluid Mech. **377**, 223–252 (1998).
[19] K. Dohan and B. R. Sutherland, "Internal waves generated from a turbulent mixed region," Phys. Fluids **15**(2), 488–498 (2003).
[20] J. R. Taylor and S. Sarkar, "Internal gravity waves generated by a turbulent bottom Ekman layer," J. Fluid Mech. **590**, 331–354 (2007).
[21] H. T. Pham, S. Sarkar, and K. A. Brucker, "Dynamics of a stratified shear layer above a region of uniform stratification," J. Fluid Mech. **630**, 191–223 (2009).
[22] H. Tennekes and J. L. Lumley, *A First Course in Turbulence* (The MIT Press, Cambridge, MA, 1972).
[23] P. Meunier and G. R. Spedding, "Stratified propelled wakes," J. Fluid Mech. **552**, 229–256 (2006).
[24] S. I. Voropayev, G. B. McEachern, H. J. S. Fernando, and D. L. Boyer, "Large vortex structures behind a maneuvering body in stratified fluids," Phys. Fluids **11**(6), 1682–1684 (1999).
[25] R. Pasquetti, "Temporal/spatial simulation of the stratified far wake of a sphere," Comput. Fluids **40**, 179–187 (2011).
[26] M. B. de Stadler and S. Sarkar, "Simulation of a propelled wake with moderate excess momentum in a stratified fluid," J. Fluid Mech. **692**, 28–52 (2012).
[27] I. Yavneh, "On red-black SOR smoothing in multigrid," SIAM J. Sci. Comput. **17**(1), 180–192 (1996).
[28] R. S. Rogallo, "Numerical experiments in homogeneous turbulence," Technical Report TM-81315, NASA, Ames Research Center, 1981.
[29] F. G. Jacobitz and S. Sarkar, "The effect of nonvertical shear on turbulence in a stably stratified medium," Phys. Fluids **10**(5), 1158–1168 (1998).
[30] F. G. Jacobitz and S. Sarkar, "A direct numerical study of transport and anisotropy in a stably stratified turbulent flow with uniform horizontal shear," Flow, Turbul. Combust. **63**(1), 343–360 (2000).